

GSA DATA REPOSITORY 2020151

Soleymani, H., Kidder, S., Hirth, G., and Garapić, G., 2020, The effect of cooling during deformation on recrystallized grain-size piezometry: *Geology*, v. 48, <https://doi.org/10.1130/G46972.1>

SUPPLEMENTAL MATERIAL

1. Starting material

To simulate a typical deformed rock experiencing cooling, a homogeneous starting material with relatively coarse-grain size relative to the size of recrystallized grains that would be generated during the experiment was desired. Given typical experimental recrystallized grain sizes of (3-10 μm), this meant a starting material with a grain size 10-20 μm . We synthesize such a material by sintering silica gel at 900 °C and 1.1 GPa for 24 hours. Silica gel is widely available commercially in various grain and pore sizes. Here we used commercial-grade silica gel (VWR International, West Chester, PA, USA; no. BDH9004) with 60 nm and 60-200 μm pore and grain size respectively. “As-received” silica gel can be described as high purity amorphous silica with relatively high-water content. Because of its high purity, silica gel has been used as a starting material in several experimental studies (Luan and Paterson, 1992; Nachlas, 2016; Nachlas et al., 2018). Also, the mechanical and microstructural characteristics of the synthesized silica gel have been shown to produce comparable rheological and microstructural results as natural quartzite at experimental conditions (Luth and Ingamells, 1965; Paterson and Luan, 1990; Luan and Paterson, 1992; Nachlas and Hirth, 2015; Nachlas et al., 2018).

As-received silica gel was cleaned of potential surface impurities following the cleaning and preparation procedure of Nachlas (2016). To reduce the water content, we heated the starting material at 825 °C for 1 hr in a platinum crucible using a conventional furnace, then packed this in a platinum jacket and stored it in a vacuum furnace at ~100 °C for up to two weeks. Silica gel can hold up to 12 wt% H_2O due to its interconnected hydrophobic nanopores. Based on weight loss measurements before and after heat treatment, we assume all such water was eliminated. However, an unknown amount of water was reabsorbed by silica gel from the air while transferring the material from the oven to the jacket. 0.16 gr of heat-treated silica gel was packed between a set of 45° precut and polished yttria-stabilized zirconia (ZrO_2) pistons with 1 μL of deionized H_2O (~ 0.6 wt%) placed on the surface of a piston. The sample and the pistons were placed inside a Pt jacket with a thickness of 0.127 mm and covered with a Pt disk placed at each end. The Pt jacket was then folded over the disks and placed in a Ni foil. Full mechanical sealing was achieved during the pressurization of the experiment. Solid NaCl was used as a pressure medium in all experiments (Fig S1a, b). Heat was produced by passing alternating current through a straight graphite furnace. The heat is regulated by a Pt/Pt-Rh (S-type) thermocouple in a closed-loop PID-controlled circuit.

To reach the desired pressure and temperature and maintain mechanical retention of water in the jacket, we followed the protocol described by (Chernak et al., 2009). Once the target conditions were achieved, the σ_1 piston was held ~1 mm away from the top of the forcing block, and the sample was sintered at 900 °C, 1.1 GPa confining pressure for 24 hr. During this time, amorphous silica gel begins to crystallize to form a starting quartz aggregate (Fig S1c, d). The hydrostatic hot-pressing of the silica gel at 900 °C for 24 hr promotes significant compaction and

a produces a concave surface of the jacket after sintering (Fig S1d). Optical assessment of a sample retrieved at this stage (Fig. S1C, W2145) shows heterogeneous grain growth with large grains with spherulitic structure (grain diameter $\sim 100 \mu\text{m}$) surrounded by relatively smaller grains ($> 5 \mu\text{m}$) (Fig. S1c). Similar microstructures were reported by Luan and Paterson (1992) in synthetic quartzite and have also been observed in natural quartz associated with hydrothermal gold deposits (Herrington and Wilkinson, 1993).

Following sintering, a rotary AC motor equipped with a gearbox system drove the σ_1 piston through the top lead piece (i.e., “run-in”) and reached the top of the forcing block. The run-in stage of the experiment was used to estimate the frictional forces acting on the σ_1 piston and find the hit point using a graph of stress versus time (Peč, 2014). At the end of the experiments, the motor was stopped, and the temperature was decreased to 300°C within 2 min, then pressure and temperature were decreased incrementally to reach ambient conditions. The retrieved samples were covered in epoxy and cut parallel to the shear direction using a slow diamond saw.

2. Data acquisition

The applied force on the sample was measured by a load cell located along the forcing column and outside of the sample assembly. A pressure transducer similarly records the applied pressure on the sample during the experiment. Pre-calibrated transform equations were used to convert the electrical signals from the load cell and pressure transducer to units of force. Vertical displacement of the top forcing piston was measured by a direct current displacement transducer (DC-DT). Considering the purpose and relatively long duration (approximately three days) of many experiments, a sampling rate of 1 Hz was selected to record the electrical signals using an analog-digital converter (ADC).

A similar processing procedure as described by Peč (2014) was used to calculate the “hit-point” from the run-in curve and derive the corrected values of maximum stress component (σ_1), minimum stress component (σ_3), differential stress ($\Delta\sigma = \sigma_1 - \sigma_3$), and shear stress for the 45° precut piston ($\tau \approx \frac{\Delta\sigma}{2}$) (Okazaki and Hirth, 2016). Note that mechanical data were only corrected for piston friction and confining pressure changes (up to $\pm 75 \text{ MPa}$) during the experiments. We did not apply other corrections, e.g., overlapping area reduction. The Holyoke et al. (2010) solid salt correction was not applied. Shear strain and strain rate were calculated using the final thickness of the samples and assuming the sample maintained constant thickness during deformation carried out at a constant displacement rate of the σ_1 piston of $0.018 \mu\text{m/sec}$. In experiments involving silica gel, the initial hot press causes significant volume reduction and a “neck-shape” of the samples, e.g., fig S1d; Nachlas and Hirth (2015). During shear deformation, the samples underwent progressive thinning as documented by previous workers (Heilbronner and Keulen, 2006; Muto et al., 2011; Togle, 2014; Nachlas and Hirth, 2015), which complicates calculation of shear strain ($\gamma = \text{shear offset/thickness}$). Precise measurements of sample thickness and piston displacement along the shear component for the low and high strained samples showed that much of the thinning was induced during the early deformation stage (i.e., $\sim 25\%$ thickness reduction by $\gamma \approx 1$, with another 25% achieved between shear strain $\gamma \approx 1$ and $\gamma \approx 4$). Thus, calculating shear strain is based on an assumption of total conversion of axial σ_1 displacement to a shear component results in an overestimate of shear strain, especially for the low strain sample (W2112). To compare the general shear experiments with previously published axial compression experiments, shear stresses and shear strain rates were converted to equivalent stress ($\sigma_{eq} = \sqrt{3}\tau$) and strain rates ($\dot{\epsilon}_{eff} = \frac{1}{\sqrt{3}}\dot{\gamma}$) (Paterson and Olgaard, 2000).

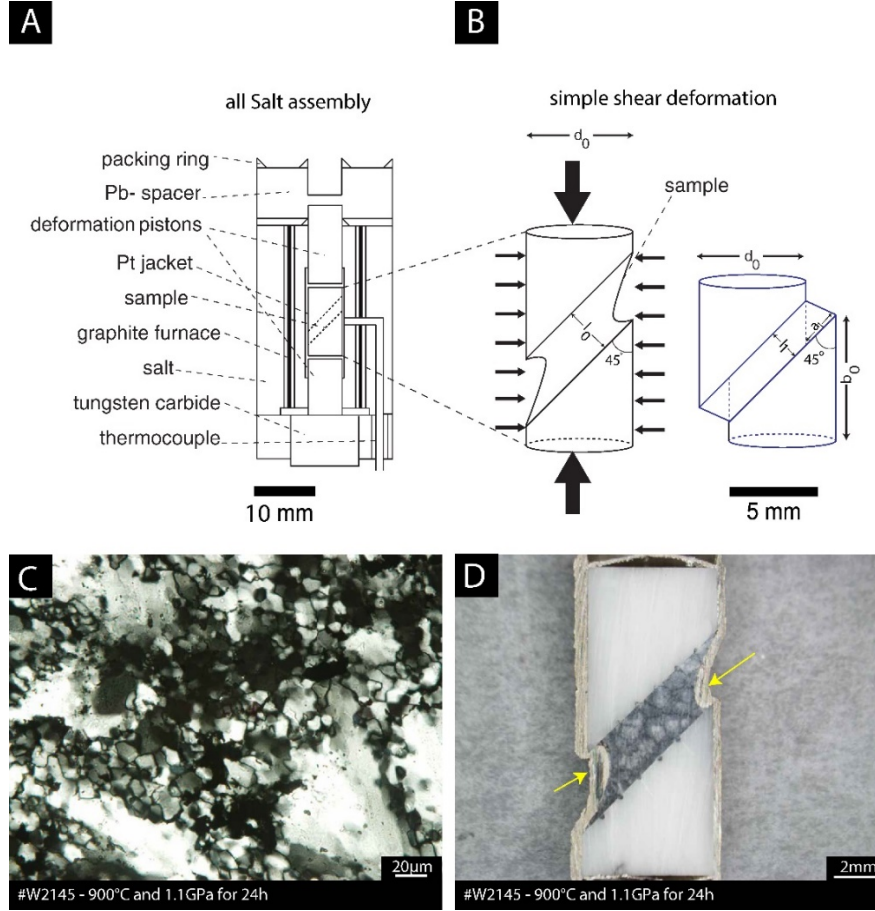


Figure. S1. Schematic drawing of solid-salt assembly and photomicrograph of hot-pressed silica gel. (A) Sample assembly consists of inner and outer solid NaCl, graphite furnace, inner Pt, outer Ni jackets, and S-type thermocouples. (B) Geometry of ideal pre- and post-deformation sample and forcing pistons. The sample is placed in between two 45° pre-cut forcing pistons. The large and small arrows show the direction of σ_1 and σ_3 ($\sigma_2 = \sigma_3$) respectively. (C) Photomicrograph of the sintered silica gel after 24 hr at 900 °C and 1.1 GPa showing heterogeneous grain size across the sample. (D) Cross section of the sample assembly after sintering stage. Note the concave surface of the jacket (yellow arrows) as a result of porosity-reduction of the starting material during heating stage.

3. Scaling of Experiments to Natural Conditions

To produce a geologically-relevant amount of recrystallization for each increment of deformation during cooling, the experimental conditions of the cooling-ramp experiments were scaled to typical geologic ratios of cooling rate to strain-rate. Scaling was carried out by equating the ratio of cooling rate over strain rate in nature and laboratory conditions as:

$$\frac{\frac{dT}{dt}_{(nature)}}{\dot{\gamma}_{(nature)}} = \frac{\frac{dT}{dt}_{(lab)}}{\dot{\gamma}_{(lab)}} \quad (1)$$

where $\frac{dT}{dt}_{(nature)}$ is a geological cooling rate calculated using various radioactive dating methods (Fig. 2 main paper), $\dot{\gamma}_{(nature)}$ is estimated geologic strain rate, $\frac{dT}{dt}_{(lab)}$ is the experimental cooling rate, and $\dot{\gamma}_{(lab)}$ is the experimental strain rate. The strain rate, and the

starting and end temperatures were selected so that deformation was carried out by crystal plasticity throughout the experiment.

The experimental cooling rates were designed to cover as wide a range of conditions as possible given experimental constraints. An impending design challenge for cooling rates slower than 2 °C/hr is the limited maximum plausible strain that can be reached by the end-temperature of 800 °C (if starting at 900 °C). Slower strain rates would also increase the experimental time and failure rate to levels that were not considered viable. The chosen cooling-ramp experiments span a range of 30-150 °C per strain unit, comparable to estimated geologic values. The 900° upper-temperature limit of the solid-salt cell is defined by the melting temperature of the NaCl confining medium. The 800 °C low-temperature limit of the experiments is defined by the stress at which grain size of quartz becomes too small to be reliably detected using EBSD (Kidder and Prior, 2014).

3.1 Evolution of recrystallized grain size during cooling in laboratory vs. nature

One can compare the relative change in steady state recrystallized grain size due to a 100 °C temperature change in the laboratory vs. nature. In our experiments there was a factor of three difference between the expected steady-state recrystallized grain size at 900 °C (~ 6 µm) and that predicted for the peak stress during strain hardening at 800 °C (~ 2 µm at the equivalent stress of $\tau \sim 180$ MPa). This is about half the relative difference expected for natural quartz deformed while cooling from 450 to 350 °C at a typical geologic strain rate of 10-13 s⁻¹ (~ 65 to ~ 11 µm using the flow law from Kidder et al. (2016)).

4. EBSD processing and microstructural analysis

Double polished thin sections were prepared with thicknesses less than ~20 µm. The preparation procedure included a 0.2 µm polish followed by 0.05 µm alumina powder slurry on a rotating polishing wheel. Damage to the top few nanometers was removed by vibropolishing the sample for 3 hr using a colloidal silica slurry under 400 gr weight. Quartz crystallographic orientation data was acquired from carbon coated (10 µm) thin sections with the VEGA3 Tescan SEM with tungsten filament at SUNY New Paltz. An Oxford Instrument EBSD system equipped with Aztec software was used at a working distance of 16-18 mm, step size 0.15 µm (W2143), 0.2 µm (W2142, 2139, 2141,2134,2136), 1.0 µm (W2112), and accelerating voltage of 20 kV at high vacuum condition. EBSD maps were acquired from the central area of each sample.

The acquired data were processed and analyzed with MTEX (Hielscher and Schaefer, 2008) following the routine of Cross et al., (2017) with one difference. To reduce unwanted acquisition noise, single pixelated grains (wild spikes) were first detected and removed from the data, then Dauphiné twin boundaries were identified by $60^\circ \pm 5^\circ$ rotation around the c-axis and removed. We also discarded poorly constrained grains less than 4 pixels in size. In an additional processing step not carried out by Cross et al, (2017), we removed a small population of elongated false grains with less than 20 pixels and aspect ratios more than twice the standard deviation that form along grain boundaries due to mixed EBSP. Each map was visually inspected throughout this process to verify satisfactory grain identification. To calculate grain size, we used the diameter of the equivalent circle with the same area as the grain (area equivalent diameters). Cross et al. (2017) proposed using grain orientation spread (GOS) as a proxy for intergranular dislocation density. GOS is defined as average misorientations of each point within a grain with respect to

the mean orientation of the grain. This method deconvolves the two populations of recrystallized and relic grains by finding a cut off GOS value. The cut off GOS value defined as the knee in the plot of cumulative number of grains vs GOS. The cut off GOS value associated with knee is used to distinguish likely relic (higher than knee) and recrystallized grains (lower than knee). All reported mean grain sizes are root mean square averages of grain diameter (Table S1).

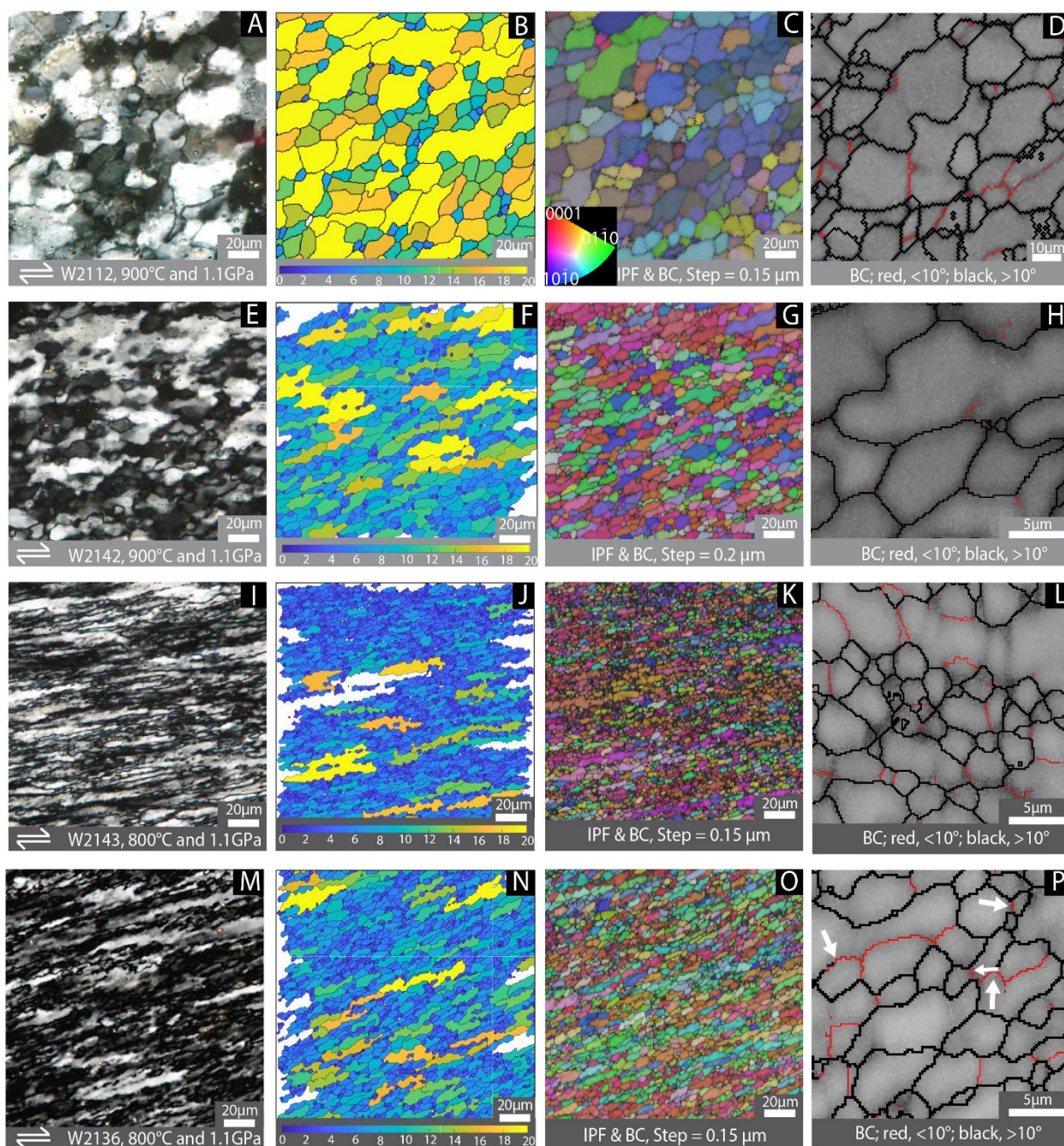


Figure S2. Photomicrographs (column 1), grain size maps (column 2), Inverse Pole Figure EBSD maps (column 3), and band contrast images (column 4) of control samples. Low-strain, 900 °C sample W2112 has large grains, occasional interlobate grain boundaries, and abundant subgrains. Note the scale difference between this sample and the others. Sample W2142 (900°C, $\gamma \approx 4$) is finer-grained than W2112 and shows a similarity between subgrain and recrystallized grain sizes. Sample W2143 (800°C, $\gamma \approx 4$) shows small bulges along high angle grain boundaries (center of L), elongated grains and subgrains. Sample W2136 (deformed entirely at 800°C) has relatively larger grain sizes than sample W2143. White arrows (P) point at low angle boundaries with visible transitions from low- to high- angle boundaries. Due to small grain size (median grain size 3 μm), optical microscopy cannot resolve many individual grains, however, bulges along the grain boundaries and internal low angle boundaries in samples W2136, W2143 are discernible from EBSD maps. Sense of shear in all images is dextral. Photomicrographs and EBSD maps are not from identical areas.

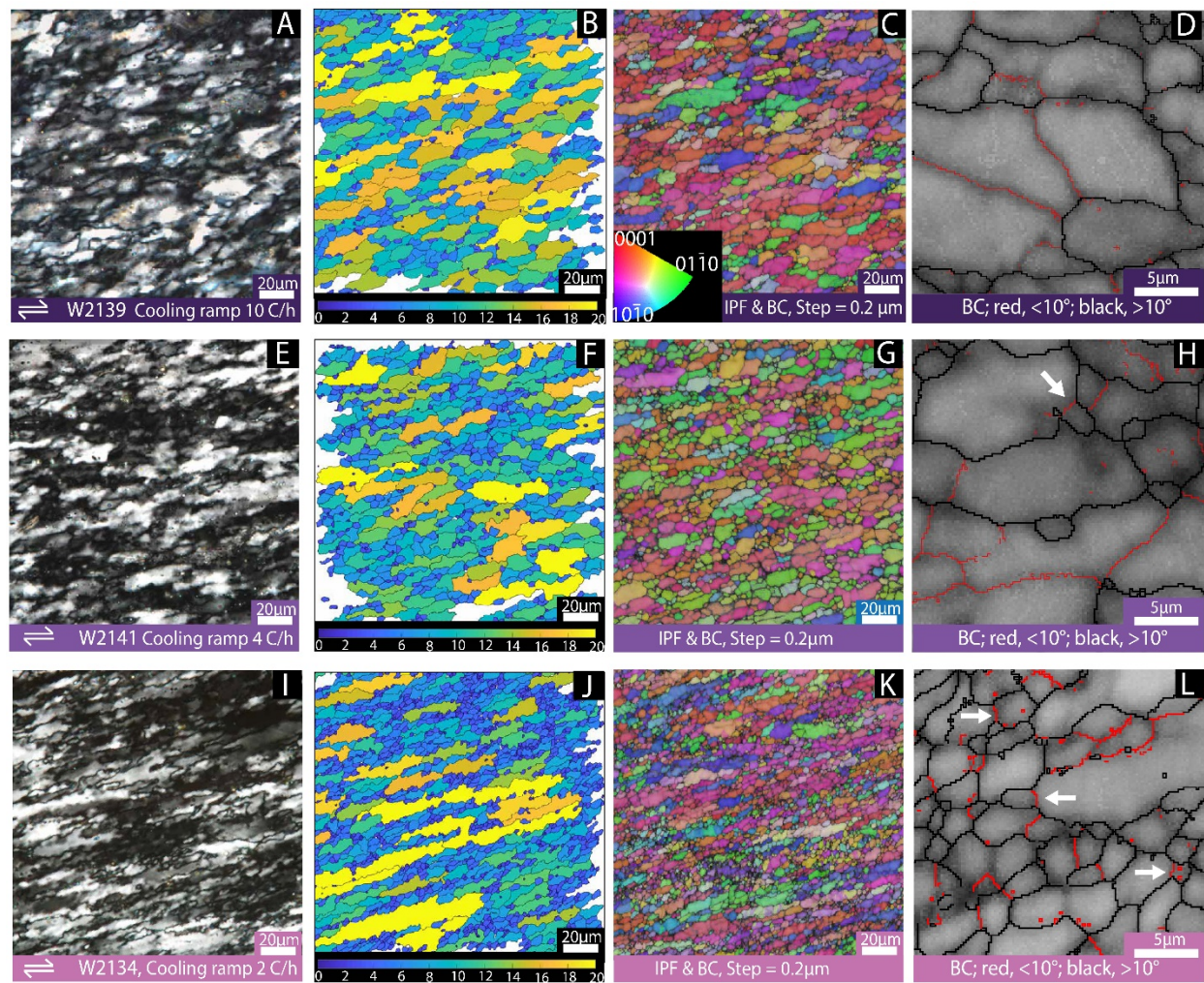


Figure S3. Photomicrographs (column 1), grain size maps (column 2), Inverse Pole Figure EBSD maps (column 3), and band contrast images (column 4) of control samples. Sample W2139 and W2141 continuously deformed while temperature decreased from 900°C to 800°C at 10 and 4°C/hr. Both samples show a comparable grain size as the control samples at 900°C, with evidence of mobile grain boundaries and subgrain rotation. Sample W2141 shows sporadic bulging and bridging subgrain boundaries as shown by the white arrow (H). The size and frequency of bulges are greater in the sample deformed at a cooling rate of 2°C/hr (L). Also, sample W2134 show a larger population of small recrystallized grains compared to faster ramps, presumably due to longer time spent at high stress conditions. Considering frequent bulging nucleation, the small recrystallized grains are likely “detached grains” formed during the final stages of deformation at high stress conditions.

TABLE S1. Summary of the experimental conditions with additional grain statistics not given in text, total area (μm^2), number of relic grains, mean relict g.s (μm), total area rxld (μm^2), and median aspect ratios of relic and recrystallized grains. Abbreviations: γ , shear strain; τ , shear stress; g.s, grain size; stdev, standard deviation; GOS, grain orientation spread; apparent τ , shear stress calculated from recrystallized grains using Cross et al. (2017); Ave τ , the average shear stress calculated over the final 80% of the experiment. Mean grain size and recrystallized grain size are root mean square averages of grain diameters.

Sample number	W2112	W2142	W2139	W2141	W2134	W2143	W2136
Max T ($^{\circ}\text{C}$)	900	900	900	900	900	800	800
Min T ($^{\circ}\text{C}$)	-	-	800	800	800	-	-
Cooling rate ($^{\circ}\text{C}/\text{h}$)	-	-	10	4	2	-	-
Ave τ (MPa)	73	82	93	99	108	144	97
Apparent τ (MPa)	51	90	85	89	118	124	107
Number of grains	954	626	796	612	2691	1833	1649
EBSd map area (μm^2)	13204	3809	5256	3784	11259	6520	7554
Number of relic grains	163	149	200	612	632	374	368
Mean relict g.s (μm)	21.75	10.70	11.70	7.25	8.43	6.33	8.17
Mean rxld g.s (μm)	13.48	5.39	5.92	5.49	3.49	3.23	4.06
Total area rxld (μm^2)	9911	2338	3087	2259	6621	4419	4794
Rxld fraction area	0.75	0.61	0.59	0.60	0.59	0.68	0.63
Med. APR relict	2.00	2.40	2.41	2.28	2.44	2.13	2.39
Med. APR rxld	1.51	1.53	1.78	1.54	1.56	1.47	1.63

SUPPLEMENTAL MATERIAL REFERENCES

- Chernak, L.J., Hirth, G., Selverstone, J., and Tullis, J., 2009, Effect of aqueous and carbonic fluids on the dislocation creep strength of quartz: *Journal of Geophysical Research: Solid Earth*, v. 114.
- Cross, A.J., Prior, D.J., Stipp, M., and Kidder, S., 2017, The recrystallized grain size piezometer for quartz: An EBSD-based calibration: *Geophysical Research Letters*, v. 44, p. 6667–6674, doi:10.1002/2017GL073836.
- Heilbronner, R., and Keulen, N., 2006, Grain size and grain shape analysis of fault rocks: *Tectonophysics*, v. 427, p. 199–216, doi:10.1016/j.tecto.2006.05.020.
- Herrington, R.J., and Wilkinson, J.J., 1993, Colloidal gold and silica in mesothermal vein systems: *Geology*, v. 21, p. 539–542, doi:10.1130/0091-7613(1993)021<0539:CGASIM>2.3.CO;2.
- Hielscher, R., and Schaebe, H., 2008, research papers A novel pole figure inversion method: specification of the MTEX algorithm research papers: , p. 1024–1037, doi:10.1107/S0021889808030112.
- Holyoke, C.W., Kronenberg, A.K., Holyoke III, C.W., Kronenberg, A.K., Holyoke, C.W., and Kronenberg, A.K., 2010, Accurate differential stress measurement using the molten salt cell and solid salt assemblies in the Griggs apparatus with applications to strength, piezometers and rheology: *Tectonophysics*, v. 494, p. 17–31, doi:10.1016/j.tecto.2010.08.001.
- Kidder, S., and Prior, D., 2014, Reversed scan direction reduces electron beam damage in EBSD maps: *Journal of microscopy*, v. 255, p. 89–93.
- Luan, F.C., and Paterson, M.S., 1992, Preparation and deformation of synthetic aggregates of quartz: *Journal of Geophysical Research: Solid Earth*, v. 97, p. 301–320.
- Luth, W.C., and Ingamells, C.O., 1965, Gel preparation of starting materials for hydrothermal experimentation: *American Mineralogist*, v. 50, p. 255–+.
- Muto, J., Hirth, G., Heilbronner, R., and Tullis, J., 2011, Plastic anisotropy and fabric evolution in sheared and recrystallized quartz single crystals: *Journal of Geophysical Research: Solid Earth*, v. 116, p. 1–18, doi:10.1029/2010JB007891.
- Nachlas, W.O., 2016, Precise and Accurate Doping of Nanoporous Silica Gel for the Synthesis of Trace Element Microanalytical Reference Materials: *Geostandards and Geoanalytical Research*, v. 40, p. 505–516.
- Nachlas, W.O., and Hirth, G., 2015, Experimental constraints on the role of dynamic recrystallization on resetting the Ti-in-quartz thermobarometer: *Journal of Geophysical Research: Solid Earth*, v. 120, p. 8120–8137, doi:10.1002/2015JB012274.
- Nachlas, W.O., Thomas, J.B., and Hirth, G., 2018, Titanite deformed: Experimental deformation of out-of-equilibrium quartz porphyroclasts: *Journal of Structural Geology*, v. 116, p. 207–222, doi:10.1016/j.jsg.2018.07.012.
- Okazaki, K., and Hirth, G., 2016, Dehydration of lawsonite could directly trigger earthquakes in subducting oceanic crust: *Nature*, v. 530, p. 81, doi:10.1038/nature16501.
- Paterson, M.S., and Luan, F.C., 1990, Quartzite rheology under geological conditions: Geological Society, London, Special Publications, v. 54, p. 299–307.
- Paterson, M.S., and Olgaard, D.L., 2000, Rock deformation tests to large shear strains in torsion: *Journal of Structural Geology*, v. 22, p. 1341–1358, doi:10.1016/S0191-8141(00)00042-0.
- Peč, M., 2014, Experimental investigation on the rheology of fault rocks: University_of_Basel.
- Tokle, L., 2014, Experimental investigation on the fabric evolution and strain localization of quartz with and without the presence of muscovite: UiT Norges arktiske universitet.

